Studies of the flow of air in a mixed-flow pump using numerical simulations

J Fernández[1]*, **A Marcos**[1], **R Barrio**[2], **E Blanco**[2], and **J Parrondo**[2]
[1]Dpto. de IMEM, Universidad de Extremadura, Badajoz, Spain
[2]Dpto. de Energía, Universidad de Oviedo, Gijón, Spain

The manuscript was received on 18 December 2010 and was accepted after revision for publication on 2 March 2011.

DOI: 10.1177/0957650911404645

Abstract: This article presents an investigation of the three-dimensional (3D) turbulent flow through the impeller passages and surroundings of a mixed-flow pump. Rotating passages of turbomachinery contain some very interesting and complex fluid flow phenomena. The model tested has five impeller blades mounted on a conical hub and nine stator blades in a diffuser which brings the diagonally outward flow back to the axial direction. Numerical calculations of the unsteady flow were carried out with the code Fluent, using air as the working fluid. Three models have been applied for turbulence closure: standard *k*-epsilon, renormalization group *k*-epsilon, and Reynolds stress model, using conventional wall functions near solid surfaces. For this transient 3D computation, the numerical grid has been decomposed into eight separate regions in order to process these in a parallel cluster of desktop computers. The results obtained show entirely reasonable correlations with previously published experimental data, as detailed in the performance curve comparisons and also in the numerical and experimental flow fields. These outcomes confirm that such a complex transient phenomenon may be reasonably captured by means of a commercial computational fluid dynamics code.

Keywords: mixed-flow pump, numerical simulations, LDA measurements, post-rotation

1 INTRODUCTION

At the present time, computational fluid dynamics programs constitute a very useful tool for the design and analysis of fluid turbomachinery and also for the prediction of global performance characteristics. The numerical analysis of turbomachines usually implies full three-dimensional (3D) flow calculations. This type of simulation should include turbulent effects, secondary flows, unsteady phenomena, etc., since the geometry of the machine is usually quite complex [**1**–**4**]. When the motion of the rotor is included, the unsteady nature of the flow generates an unsteady interaction with the stator whose effects manifest in the performance of the turbomachine. Also, this interaction brings about pressure pulsations that propagate through the hydraulic circuit and are able to generate unsteady loads on the mechanical parts [**3**, **4**], thus arising as one of the major sources of vibration and hydraulic noise [**5**].

This article presents a numerical simulation of a mixed-flow pump with a single rotor–stator stage by means of the commercial code Fluent [**6**]. The main purpose of the investigation is to calculate the global flow through the machine and also to validate the methodology developed and the numerical predictions with available experimental data. The simulation is carried out including full 3D unsteady flow calculations in order to account for the effect of the rotor–stator interaction. The dependence of the numerical predictions with respect to grid and time step size and also to turbulence model is analysed. This particular mixed-flow pump is selected because an exhaustive set of experimental data is available after the research carried out by Carey *et al.* [**7**]. They obtained the spatial distribution of several

*Corresponding author: Universidad de Extremadura, Dpto. de IMEM, Avda. de Elvas s/n, 06006 Badajoz, Spain.
email: ffrancos@unex.es

components of the velocity and also the turbulent velocity component in the axial direction by means of laser Doppler anemometry measurements.

2 NUMERICAL MODEL AND COMPUTATIONAL METHODOLOGY

The test pump was built at the University of Strathclyde in collaboration with the National Engineering Laboratory. A full and detailed description of the pump model, research facility, instrumentation, and measurement methods used is given in reference [**7**]. This is a mixed-flow pump that was tested with air, giving nominal performance values of 1.01 m^3/s and 250 Pa at 1200 r/min. The non-dimensional specific speed is $n_s = 2.5$ or, similarly, 6832 in US units (r/min, gal/min, and ft). A section through the axis can be seen in Fig. 1. The pump has five rotor blades and nine stator blades. The half-span rotor outlet diameter is 430 mm, the maximum internal casing diameter is 536 mm, and the rotor blade chord at mid-span is 280 mm. Main blade impeller and stator dimensions are summarized in Table 1.

Flow enters the machine axially through the bell-mouth inlet. There are no inlet guide-vanes, so that the fluid is drawn directly into the rotor. Both the hub of the impeller and the casing of the pump have a conical geometry. The fluid enters an unbladed passage from the impeller outlet and flows towards a stator-diffuser which also has conical hub and casing profiles. The flow is then discharged into an outlet duct. Figure 2 shows the unstructured surface mesh generated in a region of the rotor. Since the radial space between the impeller blades and the casing (i.e. tip clearance) is 0.8 mm, this gap was not included in the model in order to avoid an excessive number of cells and computational time (the blades were extended up to the casing). The total number of cells in the whole geometry is about three million. Although the structure of the grid does not allow investigating boundary layer variables, it is adequate enough for the purpose of this study, as will be shown.

The code Fluent [**6**] was used to solve the numerical flow equations with air as the operating fluid. The boundary conditions imposed for the calculations were a uniform velocity distribution at the inlet and a constant static pressure at the outlet. Second-order discretizations were used to convert time dependent and convection terms to discrete values. The pressure–velocity coupling was established by means of the SIMPLE algorithm. Flow turbulent effects were simulated by means of three different models: standard k-epsilon, renormalization group (RNG) k-epsilon, and Reynolds stress model, together with standard wall functions to calculate boundary layer variables (the $y+$ value on the impeller is around 230). Surfaces between the inlet and outlet of the rotor and the rest of the pump correspond to grid interfaces. The sliding mesh technique supported in Fluent [**6**] is used to impose the relative motion of the impeller grid with respect to the inlet and the stator during the unsteady calculations. This technique uses an interpolation routine to exchange information of the cells at both sides of the interface.

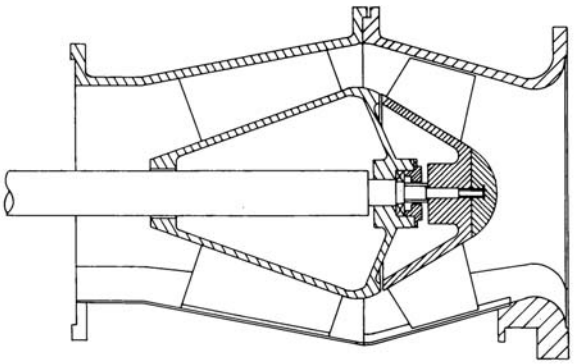

Fig. 1 Sketch of the mixed-flow pump

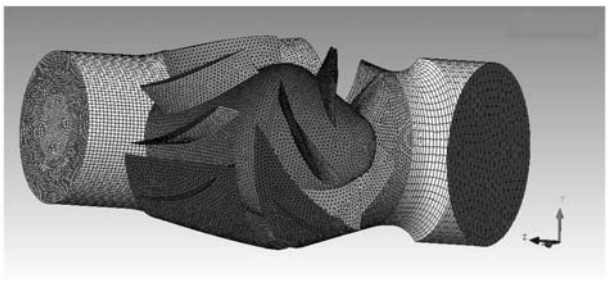

Fig. 2 Detail of the pump's surface mesh

Table 1 Principal dimensions of impeller and stator blades

	Impeller			Stator		
	r (mm)	z (mm)	β (degree)	r (mm)	z (mm)	β (degree)
Inlet (hub)	90.7	776.1	37.0	188.9	995.5	59.0
Inlet (tip)	210.9	750.0	28.6	261.6	1017.8	53.0
Outlet (hub)	177.8	913.7	46.1	91.2	1247.5	0.0
Outlet (tip)	251.9	879.0	26.7	209.9	1279.6	0.0

Steady-state calculations were carried out first by means of a frozen-rotor interface (i.e. for a given relative position of the impeller) before performing full unsteady flow simulations. Once steady convergence was achieved (the convergence criterion was the same as the one imposed for the unsteady calculations, see below), the resulting velocity and pressure fields were used as initial conditions for the unsteady computations. The time step used for the unsteady calculations was 5×10^{-4} s, which resulted in a total of 100 time steps for a single impeller revolution. The number of iterations was adjusted to reduce the magnitude of the residuals below an acceptable level in each time step. In particular, the ratio between the sum of the residuals and the sum of the fluxes for a given variable in all the cells of the mesh had to be less than 10^{-5} (five orders of magnitude). About 5–7 impeller revolutions were required to achieve a stabilized periodic regime (i.e. the flow variables became periodic over a full revolution).

The dependence of the numerical predictions with respect to grid and time step size was investigated before carrying out the bulk of the calculations. For this purpose, several grids between 0.3 and 4 million cells were generated; also, some tests were carried out for a number of time steps for one single blade passage between 10 and 35 (i.e. for a time step size between 10^{-3} and 2.86×10^{-4} s). The results of this sensitivity analysis are presented in Fig. 3. This figure shows the magnitude of the outlet static pressure (chosen as reference variable) as a function of the number of time steps (top x-axis, right y-axis), and also of the number of cells (bottom x-axis, left y-axis). The pressure is shown normalized by the magnitude obtained with either the finest grid or the smallest time step size.

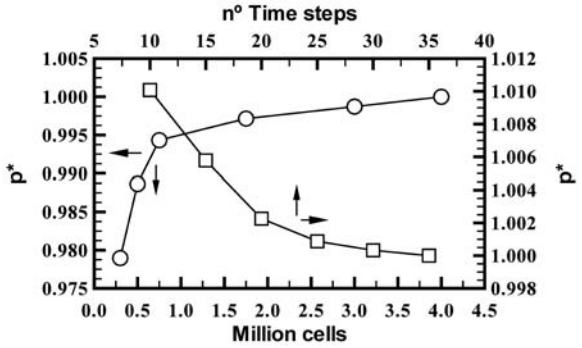

Fig. 3 Results of grid and time dependence analysis

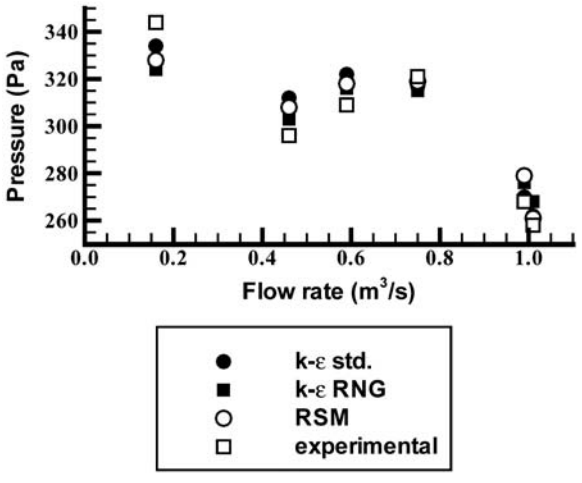

Fig. 4 Numerical and experimental performance curve

As seen, the differences in the outlet static pressure obtained for the meshes tested are small. The relative difference is about 2.1 per cent for the coarsest mesh (around 300 000 cells), whereas this difference is about 0.5 per cent for the mesh used in the final calculations (about 3 000 000 cells). The time-step dependence analysis presents similar results, even showing smaller variations in p^* than those previously indicated: it is seen that the relative change in p^* for the whole range tested remains below 1 per cent. Particularly, this variation is about 0.3 per cent for the number of time steps used in the final calculations (20 time steps for one blade passage).

3 EXPERIMENTAL VALIDATION

The numerical simulations were carried out with air for the pump running at 1200 r/min and for four points of operation: the nominal flowrate (1.010 m^3/s) and three lower flowrates (0.743, 0.593, and 0.460 m^3/s, respectively). Figure 4 shows a comparison between the experimentally determined performance characteristics and the predictions from the numerical model. The numerical pressure was obtained by averaging over one full impeller revolution (i.e. 100 samples).

As seen, the curves obtained with the three turbulence models tested match the experimental one reasonably well. Some differences are observed at the lower flowrates in the stall area, which can be attributable to the inherent difficulty in capturing this phenomenon with numerical models.

4 ANALYSIS OF NUMERICAL RESULTS

Figure 5 presents a sketch of the rotor. This sketch shows the surfaces where numerical and experimental results are compared and also the reference system used for the velocities. More details about the geometry of these surfaces can be found in reference [**7**].

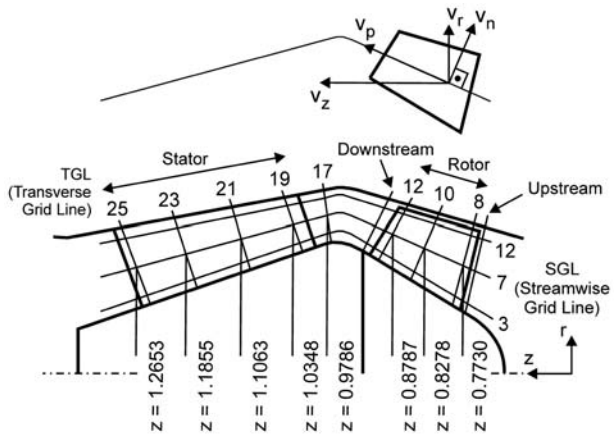

Fig. 5 Sketch of measurement sections and velocities

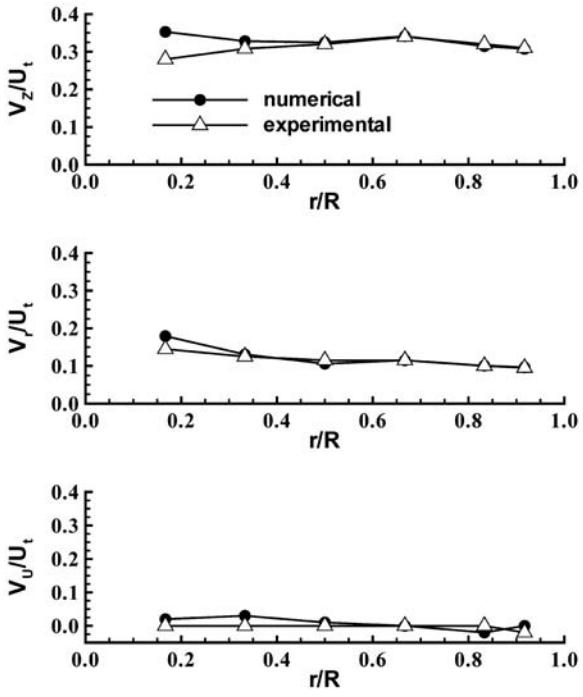

Fig. 6 Axial, radial, and tangential velocity component upstream of the rotor (from top to bottom)

Figures 6 and 7 show the spatial distribution from the hub to the casing of the circumferentially averaged axial, radial, and tangential velocity components in two positions. One of these positions is located upstream of the rotor at 16 mm before the leading edge of the blades, whereas the other position is located at 5 mm after the trailing edge (see indications in Fig. 5). The velocities are normalized by the blade's velocity at the mid-point of the trailing edge. Since the Mach number is well below 0.3 and the pressure increment along the pump is small (Fig. 4), air compressibility effects were not considered.

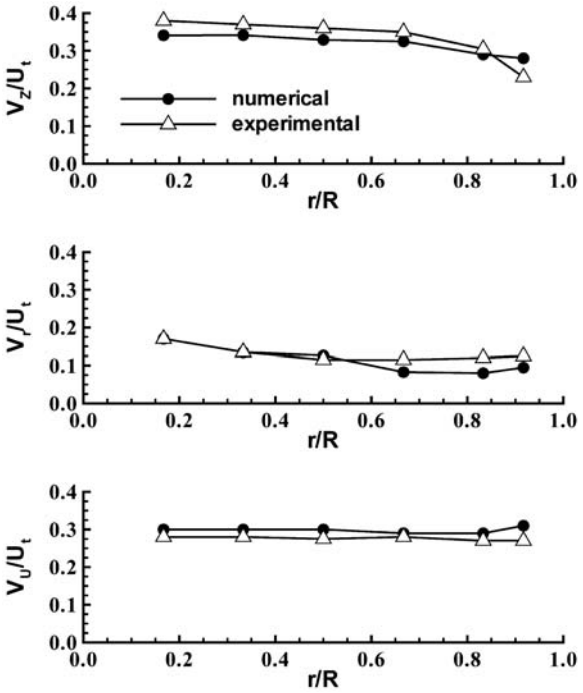

Fig. 7 Axial, radial, and tangential velocity component downstream of the rotor (from top to bottom)

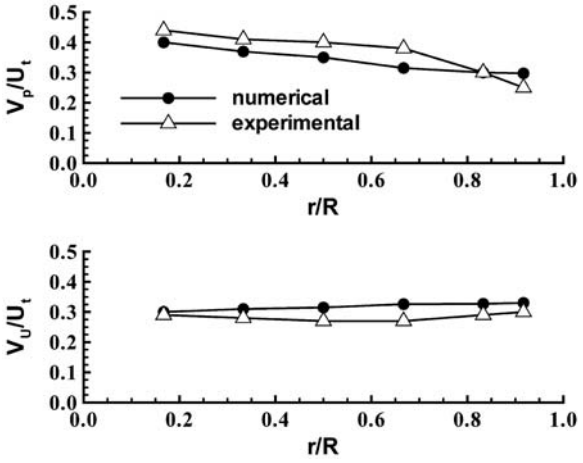

Fig. 8 Parallel to SGL and tangential velocity component downstream of the rotor Note: SGL, streamwise grid line

Upstream the leading edge (Fig. 6), it can be seen that the flow has not experienced a pre-rotation, only excluding a small region close to the hub. The flow changes its direction due to hub presence; thus, increasing the radial velocity component. This component is higher near the hub while its magnitude is progressively reduced towards the casing. The axial velocity component presents the same tendency due to the flow contraction at the inlet of the rotor. It is observed in Fig. 6 that the numerical results are in good agreement with the experiments.

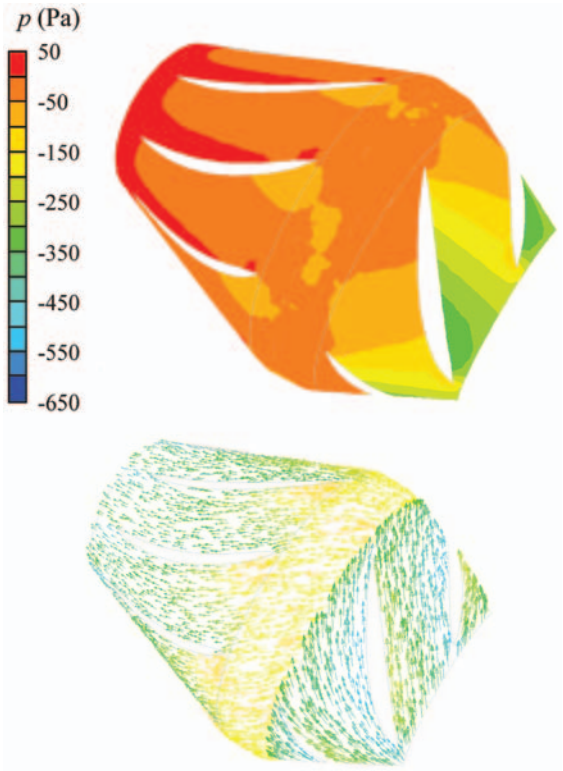

Fig. 9 Contours of instantaneous pressure and velocity vectors in the section SGL3 at nominal flowrate

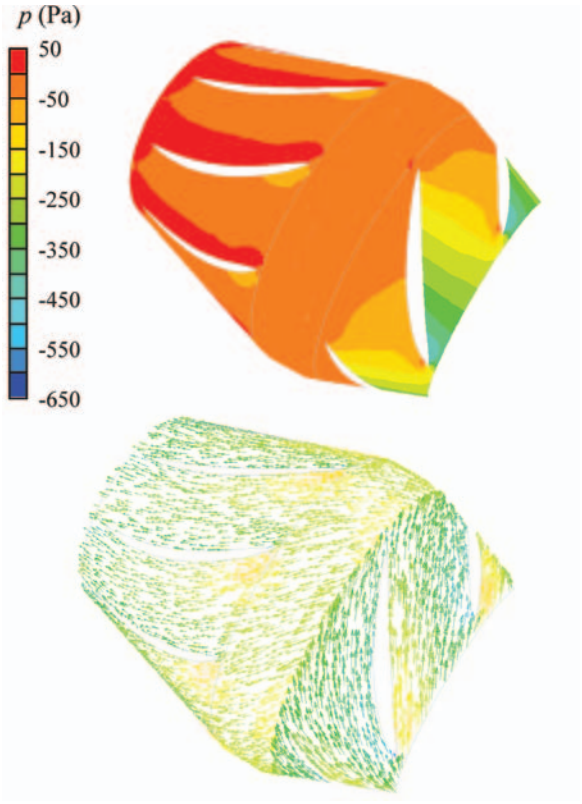

Fig. 10 Contours of instantaneous pressure and velocity vectors in the section SGL7 at nominal flowrate

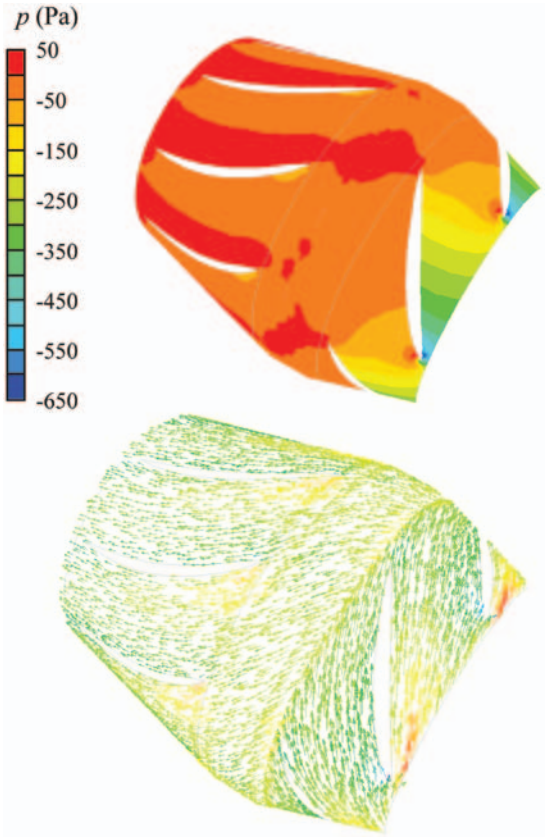

Fig. 11 Contours of instantaneous pressure and velocity vectors in the section SGL12 at nominal flowrate

Downstream the trailing edge (Fig. 7), it is seen that the flow experiences a post-rotation due to the effect of the rotor blades. The tendency of the velocity distributions is similar to that observed upstream the leading edge. In the present case, however, it is seen that there are large differences between numerical and experimental results. This can be attributable to the difficulty for the numerical models to capture the wake shed, which would require a special refinement of the mesh in that area. These differences have been partially smothered near the stator, as can be seen in Fig. 8 ($\boldsymbol{V}_{\mathrm{p}} = \boldsymbol{V}_z + \boldsymbol{V}_{\mathrm{r}}$ is used due to the experimental data available).

Figures 9 to 11 show several pictures of the instantaneous pressure contours and velocities obtained in the numerical simulations. These results are presented along pseudo-streamline surfaces for the nominal flowrate (1.010 m^3/s). A relative frame of reference was used for the vectors in the rotor; downstream the rotor, the velocity vectors are defined with respect to an absolute frame of reference. Comparisons with experimental results at some specific locations (Fig. 5) are shown in the following figures.

Figures 12 to 14 present the blade-to-blade variation along three conical surfaces between the hub and

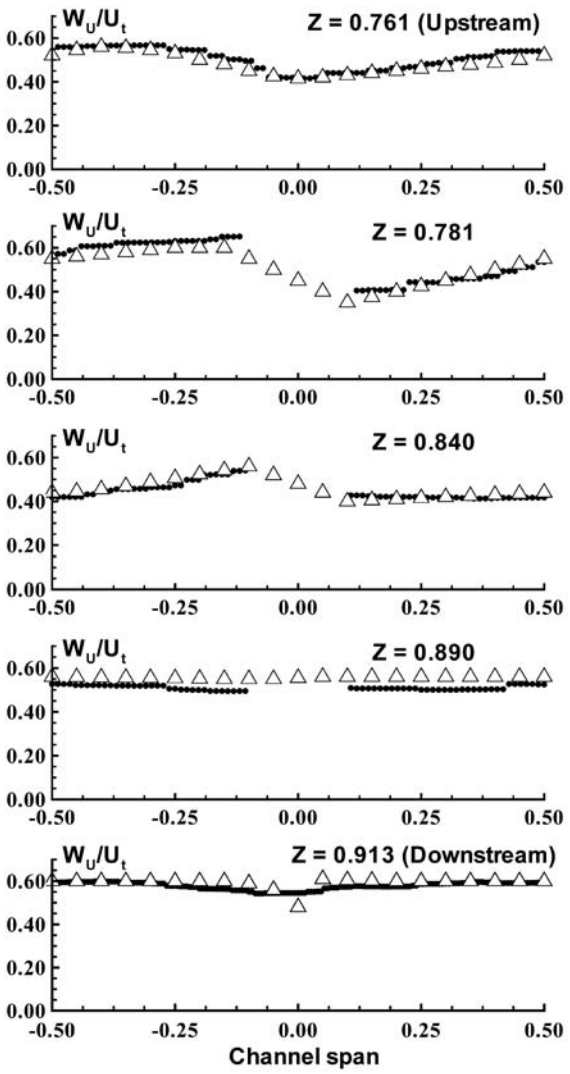

Fig. 12 Blade-to-blade variation of the relative tangential velocity in the section SGL3 (triangles represent the experimental data)

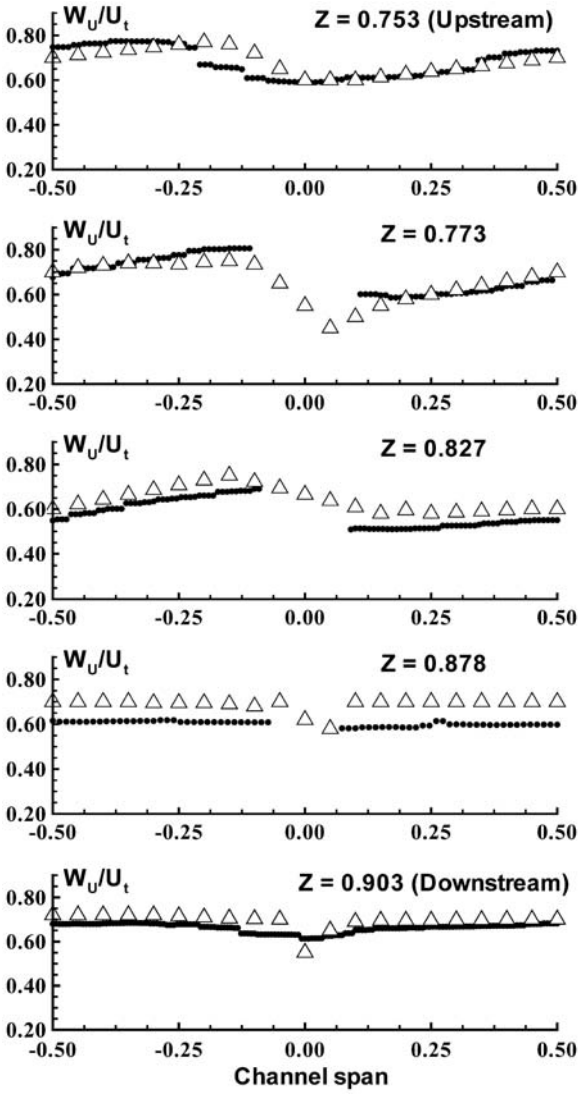

Fig. 13 Blade-to-blade variation of the relative tangential velocity in the section SGL7 (triangles represent the experimental data)

the casing of the tangential component obtained from the relative velocity in the rotor. The position $x = 0$ is located in the blade centre-line, with the suction surface to the left ($x < 0$). Each figure contains curves giving the numerical (circles) and experimental values (triangles) at five axial positions.

As observed, there is a variation in the tangential component of the velocity across the blade leading edge upstream of the impeller, which induces a change in the angle of the relative flow. The distortion of the flow is higher in the casing region, where there is a more significant variation from the pressure to the suction side. Within the blade passage, the variations in the magnitude of W_u across the blade pitch are larger near the leading edge than near the trailing edge. In the middle of the blade passage, variations in the tangential velocity can be observed only close to the suction side.

The principal feature of the flow downstream of the impeller is the wake shed from the trailing edge of the blades. The transport and dissipation of the wake is accompanied by diffusion and mixing of the flow. The numerical results obtained near the casing are worse because the grid size in this region is not adequate for a precise boundary layer calculation. It would be necessary to build a structured grid in this area with the purpose of solving the equations with an enhanced treatment.

Some results of the stator velocity profiles are presented in Fig. 15. Although there are less experimental measurement locations, the numerical results still show a relatively good agreement with the experiments. It can be clearly seen that the circumferential velocity component V_u decreases through the stator, which is associated to pressure recovery.

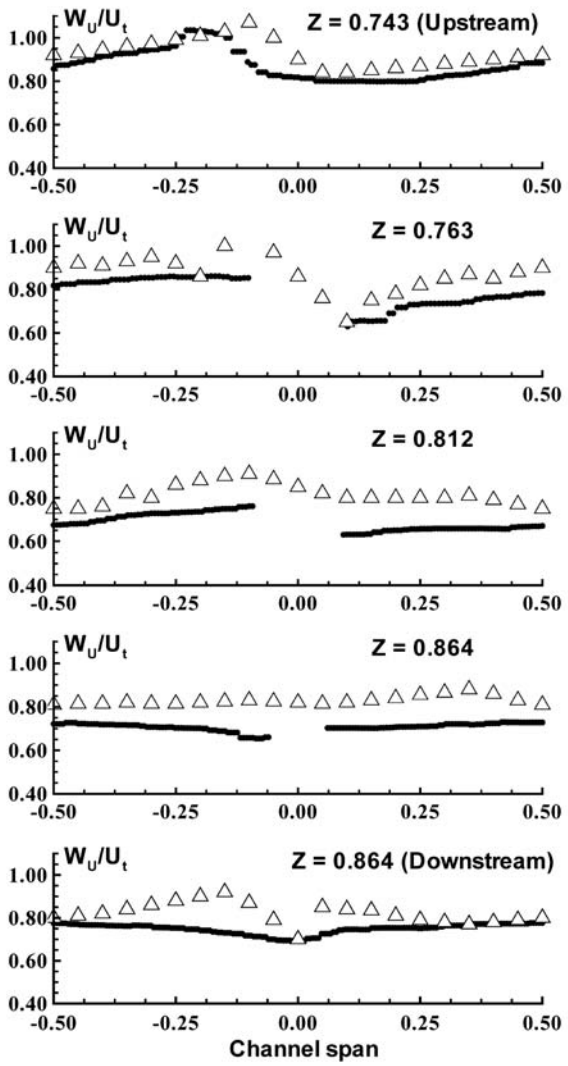

Fig. 14 Blade-to-blade variation of the relative tangential velocity in the section SGL12 (triangles represent the experimental data)

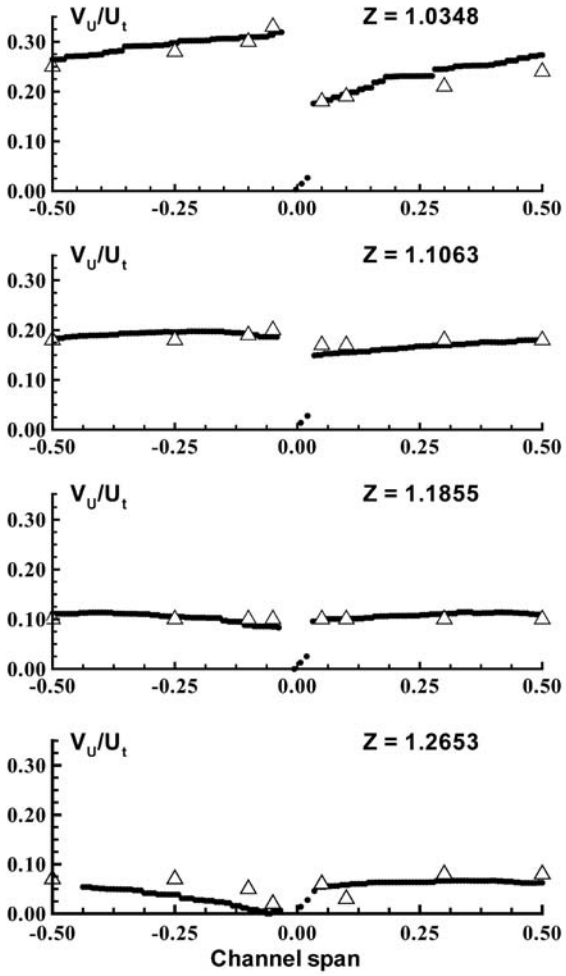

Fig. 15 Blade-to-blade variation of the tangential velocity in the section SGL7 in the stator (triangles represent the experimental data)

5 CONCLUSIONS

The performance of a conventional mixed-flow pump was numerically investigated by means of the software code Fluent. This work was carried out with full unsteady 3D flow simulations in addition to the sliding mesh technique provided by the numerical code to account for the effect of impeller–casing interactions. The purpose of the investigation was to predict the global performance characteristics of the pump.

The comparison between the numerical predictions of the global performance and the previously collected experimental data showed, in general, a good agreement. Additionally, it was found that the model overpredicted the magnitude of the pressure generated because the volumetric and mechanical losses were not included in the simulations. The presence of a tangential velocity component at the exit of the impeller for all the test flowrates could be also observed from the predictions.

FUNDING

The authors gratefully acknowledge the financial support of the Junta de Extremadura (Spain) and Feder under project PDT09A014.

REFERENCES

1 **Shi, F.** and **Tsukamoto, H.** Numerical study of pressure fluctuations caused by impeller-diffuser interaction in a diffuser pump stage. *ASME J. Fluids Engng.*, 2001, **123**, 466–474.
2 **Byskov, R. K., Jacobsen, C. B.,** and **Pedersen, N.** Flow in a centrifugal pump impeller at design and off-Design conditions—part II: Large eddy simulations. *ASME J. Fluids Engng.*, 2003, **125**, 73–83.

3 **Majidi, K.** Numerical study of unsteady flow in a centrifugal Pump. *ASME J. Turbomach.*, 2005, **127**, 363–371.
4 **Zhang, M.** and **Tsukamoto, H.** Unsteady hydrodynamic forces due to rotor-stator interaction on a diffuser Pump With identical number of vanes on the impeller and diffuser. *ASME J. Fluids Engng.*, 2005, **127**, 743–751.
5 **Dong, R., Chu, S.,** and **Katz, J.** Effect of modification to tongue and impeller geometry on unsteady flow, pressure fluctuations and noise in a centrifugal pump. *ASME J. Turbomach.*, 1997, **119**, 506–515.
6 **Fluent Inc.** *User's guide*, Vol. 10, 2006, p. NH03766(Cavendish Court, Lebanon).
7 **Carey, C.** *A study of flow of air in the rotor of a model mixed-flow pump using laser Doppler anemometry*. PhD thesis, University of Strathclyde, Glasgow, 1984.

APPENDIX

Notation

g gravity (m/s^2)
H head (m)
n_s $\omega Q^{0.5}\,(p/\rho)^{-0.75}$ specific speed (non-dimensional)
p pressure (Pa)
Q flowrate (m^3/s)
r radial coordinate (m)
R casing radius (m)
U_t tangential velocity at impeller's tip (m/s)
$\boldsymbol{V}_n$ velocity component perpendicular to streamwise grid lines (m/s)
$\boldsymbol{V}_p$ velocity component parallel to streamwise grid lines (m/s)
$\boldsymbol{V}_r$ radial velocity (m/s)
$\boldsymbol{V}_u$ tangential velocity (m/s)
$\boldsymbol{V}_z$ axial velocity (m/s)
$\boldsymbol{W}_u$ relative tangential velocity (m/s)
Z axial coordinate (m)

β tangential angle (degree)
ρ fluid density (kg/m^3)
ω speed of rotation (rad/s)

Superscripts

* normalized magnitude